Hyperspectral Detection and Unmixing of Subpixel Target Using Iterative Constrained Sparse Representation

Qiang Ling, Kun Li, Zhaoxu Li, Zaiping Lin, and Jiawen Wang

***Abstract*—With great significance in military and civilian applications, subpixel target detection is of great interest in hyperspectral remote sensing. The subpixel targets usually also need to be unmixed to identify their components. Traditionally, these subpixel targets are first detected and then unmixed to obtain their corresponding abundances. Therefore, target detection and target unmixing are independently performed. However, there are potential relations between these two processes that need to be investigated. In this article, we integrate these two processes using iterative constrained sparse representation. The main idea of this algorithm is that each pixel can be linearly and sparsely represented by the prior target spectra and several background endmembers extracted from its neighborhood. Moreover, the sum-to-one and nonnegativity constraints are introduced to ensure the sparse representation coefficients to have physical meaning. Specifically, the background endmembers are automatically extracted from the local background based on an iterative process. Then, the test pixel is represented by these extracted endmembers. Finally, the detection output is determined by the total target abundance and the residuals. The main innovation of this method is that it implements detection and unmixing of subpixel target simultaneously, even if the local background is contaminated by target signals. Experiments conducted on both synthetic and real hyperspectral datasets demonstrate that the proposed detector achieves an outstanding performance on detection and unmixing.**

***Index Terms*—Constrained sparse representation (CSR), hyperspectral imagery (HSI), linear unmixing, target detection.**

I. Introduction

HYPERSPECTRAL imagery (HSI) provides rich spectral information with hundreds of amplitude values corresponding to their wavebands [1]. The continuous spectral signature for different materials is of great help in target detection and component identification. The discriminative property leads to various applications in HSI remote sensing: denoising [2], spectral superresolution [3], target detection [4], [5], spectral unmixing [6]–[8], and dimensionality reduction [9]. Among these applications, target detection and spectral unmixing are two fundamental tasks in military and civilian fields. In the application of target detection, due to the limitation of spatial resolution, the target pixels are usually mixed by several spectra corresponding to distinct materials. Target abundance is defined as the area fraction of target material. In subpixel target detection, the target size can be estimated by its abundance and the spatial resolution. In practice, the edge of the pure pixel target usually contains many subpixels with target materials. To accurately know the size of the target, these subpixels need to be unmixed to obtain their target abundance. Therefore, detection and unmixing of subpixel target to obtain its abundance has broad application prospects, especially in mineral exploration and military target detection. Traditionally, the subpixel target is first detected and then unmixed to obtain its target abundance. However, these methods, which incorporate detection process and unmixing process, are too complicated to be carried out automatically.

With the prior target spectra, HSI target detection can be regarded as a binary classifier that labels each pixel as target or background. Based on statistical hypothesis testing techniques, several classical target detection algorithms have been proposed. A spectral matched filter (SMF) [10] detects the target with the estimated background covariance and a single target spectrum. However, if multiple types of target are present in the scene, the SMF will suffer degeneration. Instead, subspace-based detectors, such as adaptive subspace detector [11] and matched subspace detector (MSD) [12], are modeled in the target subspace generated by all prior target spectra. These methods assume that the background obeys a Gaussian distribution. However, considering the spectral variability of complicated background with several materials and objects, truly Gaussian behavior rarely occurs [13]. Therefore, many machine-learning-based nonparametric methods, such as support vector machine (SVM) [14], metric learning [15], and multitask learning [16], are applied to HSI target detection.

Recently, sparse representation (SR)-based techniques have been successfully applied to HSI target detection [5], [17]–[19]. The basic SR-based detector [17] represents each test pixel as a sparse linear combination of atoms from the background

Manuscript received October 1, 2021; revised November 21, 2021 and December 19, 2021; accepted December 29, 2021. Date of publication January 5, 2022; date of current version January 20, 2022. This work was supported in part by the Shanghai Aerospace Science and Technology Innovation Fund and in part by the National Natural Science Foundation of China under Grant 62002372. *(Corresponding author: Qiang Ling.)*

Qiang Ling, Kun Li, Zhaoxu Li, and Zaiping Lin are with the College of Electronic Science and Technology, National University of Defense Technology, Changsha 410073, China (e-mail: lq910131@163.com; likun19@nudt.edu.cn; lizhaoxu@nudt.edu.cn; linzaiping@sina.com).

Jiawen Wang is with the Shanghai Institute of Satellite Engineering, China Aerospace Science and Technology Corporation, Shanghai 201100, China (e-mail: 313474093@qq.com).

Digital Object Identifier 10.1109/JSTARS.2022.3140389

dictionary or target dictionary and then detects the targets by using representation residuals. The SR-based binary hypothesis (SRBBH) detector [18] incorporates SR with binary hypothesis and separately represents the test pixel by the prior target information or local background information. The main advantage of these methods is that there is no need to make explicit assumption about the background statistical distribution [17]. However, these methods will degenerate if the background dictionary is contaminated by target pixels. A locality-constrained linear coding-based background dictionary learning (DM-BDL) method [4] is proposed to obtain a complete and compact background dictionary. Meanwhile, a total variation constraint is imposed on the representation coefficient to exploit the spatial homogeneity of the background. The hybrid sparsity and statistics (HSS) detector [19] combines SR with statistical distribution theory and also applies a purification process to handle target contamination in the background dictionary. The constrained sparse representation (CSR)-based binary hypothesis detector [5] imposes an upper bound constraint to the abundance vector. Then, these upper bounds are automatically estimated by the background information and prior target information. This algorithm also can suppress target signals that are present in the background dictionary. However, all these sparsity-based methods cannot unmix the subpixel target to obtain its target abundance.

Aiming at estimating the abundance of endmembers, HSI unmixing deals with the problem of identifying the components of mixed spectra and estimating their weights [20]. According to whether a spectral library is available or not, HSI unmixing can be classified into unsupervised unmixing and semisupervised unmixing [21]. Unsupervised unmixing [22]–[25] represents mixed pixels by endmembers extracted from the HSI scene, while semisupervised unmixing [26], [27] represents mixed pixels by endmembers from a large spectral library. In this article, we focus on the problem of detecting subpixel targets and unmixing them to obtain their corresponding abundances. Compared to traditional HSI unmixing, this problem combines unsupervised unmixing and semisupervised unmixing, where the prior target spectra are considered as target endmembers, and background endmembers need to be extracted from the local background in the scene. Note that the problem of HSI unmixing in this article is solved locally, that is, it cannot be treated as a traditional unmixing problem since, for each pixel, only a local background and the prior target spectra are available. Compared to the whole scene, the endmembers in a small region are more similar. Therefore, our method can deal with the spectral variability caused by large distance in the image plane, while literature [7] uses the augmented linear mixing model (ALMM) to deal with this problem in the whole scene.

In this article, we propose an iterative constrained sparse representation (ICSR)-based algorithm to solve this problem. According to the linear mixture model [28], the sum-to-one and nonnegativity constraints are imposed on the representation coefficients to ensure their physical meaning. First, an iterative process is proposed to automatically extract only background endmembers from the local background. It is not required to estimate the number of endmembers in the local background, which is a difficult problem for unsupervised unmixing. Then, the test pixel is separately represented by different endmembers under the binary hypotheses in [18]. Finally, the detection output is determined by multiplying the total target abundance with the residuals. The main contributions of this article are summarized as follows.

1) *On the whole:* The proposed method incorporates target detection and target unmixing into a united framework such that it can detect targets and obtain the abundances of the detected targets simultaneously, even if some target pixels contaminate the background dictionary. In this way, it obtains the area proportion of the targets and, thus, has a broad application prospect.
2) *Target detection:* We propose a novel detector to exploit both reconstruction residual information and abundance information of each test sample to enhance the difference between the target and the background and, thus, obtain better detection performance.
3) *Target unmixing:* The proposed method extracts the background endmembers from a very small local background centered at the target pixel when the target is unmixed. Compared with the unmixing methods that extract the endmembers on the whole HSI and then estimate the target abundances, the proposed algorithm is more robust to the spectral variability of the background and can extract more accurate target abundance.

The rest of this article is organized as follows. Two previous algorithms are introduced in Section II. The proposed ICSR algorithm is described in Section III. Experiments are presented in Section IV. Finally, Section V concludes this article.

II. Previous Algorithms

In this section, we briefly review two previous algorithms for hyperspectral target detection: the SVM and the SR-based detector.

A. SVM for Target Detection

The SVM algorithm [29] can be used to solve a supervised binary classification problem for target detection in HSI. Given two classes of training samples $\boldsymbol{a}_i (i = 1, \ldots, N)$ and their corresponding label vector $\boldsymbol{l} (l_i \in 1, -1)$, the SVM aims to find the optimal hyperplane $\boldsymbol{w}^{\mathrm{T}}\boldsymbol{x} + b = 0$ to separate the samples with the largest margin by solving the following optimization problem:

$$\begin{aligned} \min_{\boldsymbol{w},b,\boldsymbol{\xi}} \quad & \frac{1}{2}\boldsymbol{w}^{\mathrm{T}}\boldsymbol{w} + C\sum_{i=1}^{N}\xi_i \\ \text{s.t.} \quad & l_i(\boldsymbol{w}^{\mathrm{T}}\phi(\boldsymbol{a}_i) + b) \geq 1 - \xi_i \\ & \xi_i \geq 0,\ i = 1, \ldots, N \end{aligned} \tag{1}$$

where C is a regularization parameter, ξ_i are slack variables, and ϕ is a nonlinear function, which maps the samples into a higher dimensional feature space. Due to the possible high dimensionality of $\boldsymbol{w}$, the following Lagrange dual problem is

solved:

$$\begin{aligned} \min_{\boldsymbol{\alpha}} \quad & \frac{1}{2}\boldsymbol{\alpha}^{\mathrm{T}}\boldsymbol{Q}\boldsymbol{\alpha} - \boldsymbol{e}^{\mathrm{T}}\boldsymbol{\alpha} \\ \text{s.t.} \quad & \boldsymbol{l}^{\mathrm{T}}\boldsymbol{\alpha} = 0 \\ & 0 \le \alpha_i \le C,\ i = 1, \ldots, N \end{aligned} \tag{2}$$

where $\boldsymbol{e}$ is an $N \times 1$ vector of all ones, $\boldsymbol{Q}$ is an $N \times N$ positive-semidefinite matrix with each entry $Q_{ij} = l_i l_j k(\boldsymbol{a}_i, \boldsymbol{a}_j)$, and $k(\boldsymbol{a}_i, \boldsymbol{a}_j) = \phi(\boldsymbol{a}_i)^{\mathrm{T}}\phi(\boldsymbol{a}_j)$ is the kernel function. The commonly used Gaussian radial basis function kernel $k(\boldsymbol{a}_i, \boldsymbol{a}_j) = \exp(-\gamma\|\boldsymbol{a}_i - \boldsymbol{a}_j\|_2^2)$ is adopted as the kernel function in this article. Then, the dual problem is solved by a fast sequential minimal optimization (SMO) decomposition method [30].

After the dual problem being solved, the optimal solution $\hat{\boldsymbol{\alpha}}$ can be obtained. Then, using the primal–dual relationship, the detection value of a test sample $\boldsymbol{y}$ is calculated by

$$D_{\mathrm{SVM}}(\boldsymbol{y}) = \hat{\boldsymbol{w}}^{\mathrm{T}}\phi(\boldsymbol{y}) + \hat{b} = \sum_{i=1}^{N} l_i \hat{\alpha}_i K(\boldsymbol{a}_i, \boldsymbol{y}) + \hat{b} \tag{3}$$

where $\hat{b}$ can be computed from $\hat{\alpha}_i$, which satisfies $0 < \hat{\alpha}_i < C$; detailed explanation can be found in [31].

B. SR for Target Detection

In the sparsity-based model for HSI target detection [17], each test pixel is assumed to lie in a low-dimensional subspace spanned by background and target spectra. Therefore, it can be approximately represented as a sparse linear combination of the background and target dictionaries

$$\boldsymbol{y} \approx \boldsymbol{A}_b\boldsymbol{\alpha}_b + \boldsymbol{A}_t\boldsymbol{\alpha}_t = [\boldsymbol{A}_b\ \boldsymbol{A}_t]\begin{bmatrix}\boldsymbol{\alpha}_b \\ \boldsymbol{\alpha}_t\end{bmatrix} = \boldsymbol{A}\boldsymbol{\alpha} \tag{4}$$

where $\boldsymbol{y}$ is the test pixel and $\boldsymbol{A} \in \mathbb{R}^{M \times N}$ is the union dictionary combined by the background dictionary $\boldsymbol{A}_b$ and target dictionary $\boldsymbol{A}_t$. $\boldsymbol{A}_b$ is usually constructed by the pixels between the inner window region and the out window region of a sliding dual window centered at each test pixel [17]. $\boldsymbol{A}_t$ is constructed by the prior target spectra. M is the number of spectral bands, and $N = N_b + N_t$ is the number of atoms in $\boldsymbol{A}$. N_b and N_t are the number of atoms in $\boldsymbol{A}_b$ and $\boldsymbol{A}_t$, respectively. $\boldsymbol{\alpha}_b$ and $\boldsymbol{\alpha}_t$ are the weight vectors corresponding to $\boldsymbol{A}_b$ and $\boldsymbol{A}_t$, respectively. $\boldsymbol{\alpha}$ is a sparse vector that is constructed by concatenating $\boldsymbol{\alpha}_b$ and $\boldsymbol{\alpha}_t$.

The sparse vector $\boldsymbol{\alpha}$ can be obtained by solving the following optimization problem:

$$\min_{\boldsymbol{\alpha}} \|\boldsymbol{y} - \boldsymbol{A}\boldsymbol{\alpha}\|_2^2 \ \text{ s.t. } \|\boldsymbol{\alpha}\|_0 \le K \tag{5}$$

where $\|\cdot\|_0$ is the l_0 norm and K is the given upper bound of the sparsity level. The orthogonal matching pursuit algorithm [32] can be used to solve this problem.

This reconstruction process can lead to a competition between the background dictionary and the target dictionary. Once the optimal solution $\hat{\boldsymbol{\alpha}}$ is obtained, the reconstruction residuals via these two dictionaries are

$$\begin{aligned} r_b(\boldsymbol{y}) &= \|\boldsymbol{y} - \boldsymbol{A}_b\hat{\boldsymbol{\alpha}}_b\|_2 \\ r_t(\boldsymbol{y}) &= \|\boldsymbol{y} - \boldsymbol{A}_t\hat{\boldsymbol{\alpha}}_t\|_2 . \end{aligned} \tag{6}$$

Then, the output of this method is computed by

$$D_{\mathrm{SR}}(\boldsymbol{y}) = r_b(\boldsymbol{y}) - r_t(\boldsymbol{y}). \tag{7}$$

In practice, we usually need to unmix the subpixel target to obtain its abundance. However, the weights recovered by this sparsity model can be larger than 1 or smaller than 0, which is not physically meaningful. Meanwhile, when targets are densely distributed, some target pixels inevitably fall into the background dictionary during the sliding process of the dual window [19]. In this case, the target atoms in $\boldsymbol{A}_b$ can be used to represent the test target pixel, resulting in missing detection.

III. ICSR for Target Detection and Unmixing

In this section, we extend the basic SR-based target detection algorithm into ICSR for detecting and unmixing subpixel targets simultaneously. According to a linear mixing model [28], each test pixel can be represented as a linear combination of several endmembers weighted by their corresponding abundances. These endmembers are usually present in the local background of the test pixel or are provided by prior target spectra. The purpose of our ICSR model is to extract these endmembers and obtain their corresponding abundances. Similar to CSR for anomaly detection [33], both the sum-to-one and nonnegativity constraints are imposed on the representation coefficient $\boldsymbol{\alpha}$ in the ICSR model. Moreover, according to the Karush–Kuhn–Tucker conditions [34] for the nonnegativity constraint, the sparsity-level constraint $\|\boldsymbol{\alpha}\|_0 \le K$ is removed, where detailed explanation can refer to [33]. Then, the SR-based model defined in (5) is modified as follows:

$$\begin{aligned} \min_{\boldsymbol{\alpha}} \ & \|\boldsymbol{y} - \boldsymbol{A}\boldsymbol{\alpha}\|_2^2 \\ \text{s.t. } & \boldsymbol{e}^{\mathrm{T}}\boldsymbol{\alpha} = 1 \\ & \alpha_i \ge 0,\ i = 1, \ldots, N \end{aligned} \tag{8}$$

where $\boldsymbol{e} = [1, \ldots, 1]^T$ is an $N \times 1$ vector of all ones. Equation (8) defines a quadratic programming problem and can be effectively solved by the SMO algorithm.

However, after solving (8), the selected atoms (the atoms with nonzero weights) can be mixed pixels or may contain target signals. In this case, the weights corresponding to these selected atoms are physically meaningless. To obtain more accurate target abundances, we propose an iterative strategy. Actually, the solution of (8) by SMO is not the most sparse solution; the selected atoms usually contain many background atoms from one class with small weights.

In HSI, a pure pixel from one class cannot be linearly represented by mixed pixels or pure pixels from other classes with the sum-to-one constraint and the nonnegative constraint. Therefore, for each selected atom in $\boldsymbol{A}_b$, if it is a pure-pixel target or a subpixel target, it can be represented by the combination of the target dictionary and other selected atoms. If it is a background pixel and it cannot be effectively represented, it is a new background endmember that does not appear in the combination dictionary. Based on this property, an iterative process is designed to extract background endmembers and eliminate target signals from the background dictionary. The main idea is to remove all mixed pixels and redundant pure background pixels

from the background dictionary, leaving only one background endmember. By using the iterative strategy, pure background endmembers can be obtained, and mixed pixels in the local background can be eliminated. Meanwhile, target signals in the local background can be eliminated to obtain a pure background dictionary. Therefore, each center test pixel can be unmixed to obtain accurate target abundance and background abundance by combining the pure background dictionary with prior target dictionary.

In this iterative process, the extracted endmembers are saved in an endmember matrix $\boldsymbol{E}$, which is initialized as $\boldsymbol{A}_t$. After solving (8), the set of indices corresponding to the selected atoms in $\boldsymbol{A}_b$ is defined as Ω. For each atom $\boldsymbol{d}$ in $\boldsymbol{A}_\Omega$, if it cannot be represented by the combination of the rest of the atoms in $\boldsymbol{A}_\Omega$ and $\boldsymbol{E}$, $\boldsymbol{d}$ is considered as a new background endmember and appended to $\boldsymbol{E}$. Meanwhile, $\boldsymbol{d}$ is removed from $\boldsymbol{A}_\Omega$. Otherwise, $\boldsymbol{E}$ remains unchanged, and $\boldsymbol{d}$ is removed from $\boldsymbol{A}_\Omega$.

This process is applied to all atoms in $\boldsymbol{A}_\Omega$. Therefore, if pure-pixel targets or subpixel targets are present in $\boldsymbol{A}_\Omega$, it can be effectively represented and removed from $\boldsymbol{A}_\Omega$. The optimization problem for the kth iteration can be described as

$$\begin{aligned} &\min_{\boldsymbol{\beta}} \|\boldsymbol{d}-\boldsymbol{B}\boldsymbol{\beta}\|_2^2 \\ &\text{s.t. } \boldsymbol{e}^{\mathrm{T}}\boldsymbol{\beta}=1 \\ &\quad \beta_i \geq 0 \end{aligned} \tag{9}$$

where $\boldsymbol{B}=[\boldsymbol{A}_{\Omega_{\{k+1,\ldots,L\}}},\boldsymbol{E}]$ denotes the combination of the rest of the atoms in $\boldsymbol{A}_\Omega$ and $\boldsymbol{E}$, $\boldsymbol{d}=\boldsymbol{A}_{\Omega_k}$ denotes the kth atom in $\boldsymbol{A}_\Omega$, L denotes the number of atoms in $\boldsymbol{A}_\Omega$, and $\boldsymbol{\beta}$ is a sparse vector.

To evaluate whether $\boldsymbol{d}$ is well recovered by $\boldsymbol{B}$ or not, the root-mean-square error (RMSE) is used

$$e_{\mathrm{rms}}=\sqrt{\frac{\|\boldsymbol{d}-\boldsymbol{B}\boldsymbol{\beta}^*\|_2^2}{M}}=\frac{r}{\sqrt{M}} \tag{10}$$

where $\boldsymbol{\beta}^*$ is the optimal solution of (9), r is the recovery residual, and M is the number of spectral bands. When e_{rms} is smaller than a given threshold δ, $\boldsymbol{d}$ is considered to be well recovered and not appended to $\boldsymbol{E}$. δ denotes the threshold of the RMSE to add a new background endmember.

Then, the binary hypothesis in [18] is used. It assumes that the endmember matrix $\boldsymbol{E}$ can linearly and sparsely represent a pure target or a subpixel target, while the single background endmember matrix $\boldsymbol{E}_b$ ($\boldsymbol{E}_b=\boldsymbol{E}-\boldsymbol{A}_t$) cannot. The test pixel $\boldsymbol{y}$ is separately represented by $\boldsymbol{E}_b$ and $\boldsymbol{E}$

$$\begin{aligned} &\min_{\boldsymbol{\varphi}_b} \|\boldsymbol{y}-\boldsymbol{E}_b\boldsymbol{\varphi}_b\|_2^2 \\ &\text{s.t. } \boldsymbol{e}_b^{\mathrm{T}}\boldsymbol{\varphi}_b=1 \\ &\quad +\varphi_b^i \geq 0 \end{aligned} \tag{11}$$

$$\begin{aligned} &\min_{\boldsymbol{\varphi}} \|\boldsymbol{y}-\boldsymbol{E}\boldsymbol{\varphi}\|_2^2 \\ &\text{s.t. } \boldsymbol{e}^{\mathrm{T}}\boldsymbol{\varphi}=1 \\ &\quad \varphi^i \geq 0 \end{aligned} \tag{12}$$

where $\boldsymbol{\varphi}_b$ denotes the abundance vector corresponding to $\boldsymbol{E}_b$ and $\boldsymbol{\varphi}$ denotes the abundance vector corresponding to $\boldsymbol{E}$.

Algorithm 1: ICSR Algorithm for Detection and Unmixing of the Subpixel Target.

Input: Hyperspectral image (HSI), target dictionary $\boldsymbol{A}_t$, dual window size ($\omega_{\mathrm{in}}, \omega_{\mathrm{out}}$), parameter δ.
for each test pixel $\boldsymbol{y}$ in HSI **do**
1) Collect $\boldsymbol{A}_b$ based on ($\omega_{\mathrm{in}}, \omega_{\mathrm{out}}$), $\boldsymbol{A}=[\boldsymbol{A}_b,\boldsymbol{A}_t]$, $\boldsymbol{E}=\boldsymbol{A}_t$;
2) Solve (8) and obtain the indices $\Omega_{\{1,\ldots,L\}}$ corresponding to the atoms with nonzero weights in $\boldsymbol{A}_b$;
3) **for** $k=1,\ldots,L$ **do**
  a) $\boldsymbol{d}=\boldsymbol{A}_{\Omega_k}$, $\boldsymbol{B}=[\boldsymbol{A}_{\Omega_{\{k+1,\ldots,L\}}},\boldsymbol{E}]$;
  b) Solve (9) and obtain the recovery residual r;
  c) **if** $r/\sqrt{M}>\delta$, $\boldsymbol{E}=[\boldsymbol{d},\boldsymbol{E}]$;
end for
4) Solve (11) and (12), then obtain the optimal solutions $\boldsymbol{\varphi}_b^*$ and $\boldsymbol{\varphi}^*$;
5) Calculate the output of the detector via (14).
end for
Output: Detection map, target abundance maps.

Similarly, once the optimal solutions $\boldsymbol{\varphi}_b^*$ and $\boldsymbol{\varphi}^*$ are obtained, the reconstruction residuals can be calculated as follows:

$$\begin{aligned} r_1(\boldsymbol{y})&=\|\boldsymbol{y}-\boldsymbol{E}_b\boldsymbol{\varphi}_b^*\|_2 \\ r_2(\boldsymbol{y})&=\|\boldsymbol{y}-\boldsymbol{E}\boldsymbol{\varphi}^*\|_2. \end{aligned} \tag{13}$$

Finally, the detection value of the proposed method is calculated by multiplying the total target abundance with the residuals

$$D_{\mathrm{ICSR}}(\boldsymbol{y})=S_t(r_1(\boldsymbol{y})-r_2(\boldsymbol{y})) \tag{14}$$

$$S_t=\sum_{i=N_b'+1}^{N'}\varphi_i^* \tag{15}$$

where S_t is the total abundance of target components, N' is the number of atoms in $\boldsymbol{E}$, and N_b' is the number of atoms in $\boldsymbol{E}_b$. Given a threshold, if the detection value $D_{\mathrm{ICSR}}(\boldsymbol{y})$ of a test pixel $\boldsymbol{y}$ is larger than the threshold, $\boldsymbol{y}$ is identified as a target pixel.

If the test pixel $\boldsymbol{y}$ is a pure background pixel, $r_1(\boldsymbol{y})-r_2(\boldsymbol{y})$ is small, S_t is close to 0, and thus, the detection value $D_{\mathrm{ICSR}}(\boldsymbol{y})$ is also close to 0. If $\boldsymbol{y}$ is a target pixel or a mixed target pixel, $r_1(\boldsymbol{y})-r_2(\boldsymbol{y})$ is large, S_t is larger than 0, and thus, $D_{\mathrm{ICSR}}(\boldsymbol{y})$ is larger than 0. The higher the total target abundance S_t is, the larger $D_{\mathrm{ICSR}}(\boldsymbol{y})$ is. Consequently, the detection value differences can be amplified by multiplying the total target abundance with the residuals.

As aforementioned, parameter δ denotes the threshold of the RMSE to add a new background endmember. That means, if the RMSE between two background pixels is larger than δ, they are regarded as two endmembers. In a sense, δ is the RMSE lower bound of the two endmembers. Affected by spectral variability, nonlinear mixing effects, and noise in datasets obtained by different sensors, δ should be set to different values for different datasets. In practice, we select a small homogeneous region from the scene and calculate the RMSEs between all pixels in this region; δ is set to the maximum value of the RMSEs. Therefore, our ICSR method can only extract one endmember from this homogeneous region.

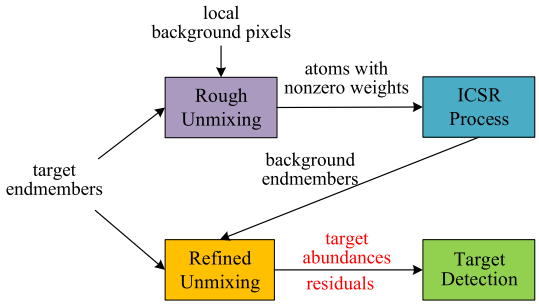

Fig. 1. Relationship between target detection and target unmixing.

In summary, the implementation details of the proposed ICSR algorithm are illustrated in Algorithm 1. The relationship between target detection and target unmixing of our ICSR method is illustrated in Fig. 1. In general, target detection is based on the results of target unmixing. In our ICSR method, target unmixing includes rough unmixing and refined unmixing. Rough unmixing provides background endmembers for refined unmixing by the ICSR process. Refined unmixing provides the target abundances and residuals for target detection. The target detection output is computed by multiplying the total target abundance with the residuals. As analyzed above, this can increase the differences between the target pixels and background pixels, resulting in better detection performance. Note that the representation coefficients of each subpixel target can also represent its area fractions due to the sum-to-one and nonnegativity constraints. Therefore, the proposed algorithm can detect and unmix the subpixel targets simultaneously. Moreover, it can purify the complicated background contaminated by target pixels and, thus, enhance the SR capability. SMO has a computational complexity ranging from $O(N)$ to $O(N^{2.2})$ for different practical problems [35]. Therefore, the computational complexity of the proposed method is about $O(N + N_t + L(L + N_t))$ to $O(N^{2.2} + N_t^{2.2} + L(L + N_t)^{2.2})$ for each pixel.

IV. Experimental Results

A. Dataset Description

The first dataset was captured by the Airborne Visible/Infrared Imaging Spectrometer (AVIRIS). It covers a part of the Salinas Valley in California, USA. This dataset has 224 spectral bands ranging from 370 to 2510 nm, with a spectral resolution of 10 nm and a spatial resolution of 3.7 m/pixel. 204 bands were retained by eliminating 20 noisy bands. The whole dataset has a size of 512×217. In this article, a subimage with a spacial size of 200×200 was selected, as shown in Fig. 2(a). This scene contains more than six different background materials: Soil-vinyard-develop, Vinyard-vertical-trellis, Corn-senesced-green-weeds, Lettuce-romaine-7wk, Lettuce-romaine-6wk, Lettuce-romaine-5wk, and so on. Twenty-five subpixel targets were planted into the real HSI. The five targets in each row have the same target material. The target materials in each column from top to bottom are Brocoli-green-weeds, Vinyard-untrained, Fallow-smooth, Stubble, and Celery, which are extracted from the area outside the selected scene. The synthetic mixed target pixels are generated based on the linear mixing model [28]. Each target has a size of 11×11 pixels, and the target abundance varies among 0.1, 0.2, 0.4, 0.6, 0.8, and 1; the abundance map of each target is shown in Fig. 2(b). There are 3025 target pixels that need to be detected and unmixed on the dataset. The target dictionary $\boldsymbol{A}_t$ is built by these five target spectra, as shown in Fig. 2(c).

The second dataset was obtained by the ProSpecTIR-VS sensor in 2012 [36]. From the geo-corrected 0920-1654 reflectance data, a subimage with a spacial size of 160×160 is selected in our experiments, as shown in Fig. 3(a). It has 360 spectral bands ranging from 400 to 2450 nm, with a spectral resolution of 5 nm and a spatial resolution of 1 m/pixel. There are two especially designed targets for unmixing in the scene. The yellow unmixing target in the upper left is generated by a 2×2 repeating pattern comprised of three yellow felt squares and one yellow cotton square, thus achieving 75% of yellow felt and 25% of yellow cotton per pixel. The blue unmixing target in the upper right alternatively consists of blue cotton squares and blue felt squares in a checkerboard fashion and, thus, achieves 50% of blue cotton and 50% of blue felt per pixel. The six fabric panels (including pink felt, yellow cotton, yellow felt, blue cotton, gold felt, and blue felt) are deployed below the unmixing targets. These eight targets with 116 pixels are used for detection performance evaluation, as shown in Fig. 3(b). The two unmixing targets are used for unmixing performance evaluation. We have extracted six endmembers from these six fabric panels in the scene as the prior target spectra, which are used to construct the target dictionary, as shown in Fig. 3(c).

The third dataset was collected by the AVIRIS sensor. It covers a naval air station in San Diego, CA, USA. This dataset has 224 spectral bands ranging from 370 to 2510 nm; 189 bands were retained by eliminating 35 noisy bands. The whole dataset has a size of 400×400. In this article a region with a size of 150×150 was selected, as shown in Fig. 4(a). There are three airplanes with 76 target pixels to be detected in the scene, as shown in Fig. 4(b). For this dataset, we extracted 3 pixels from different targets in the scene to construct the target dictionary, as shown in Fig. 4(c).

B. Robustness to Noises and Target Contamination

To quantitatively validate the robustness of our ICSR method, we investigate the detection performance and unmixing performance by adding Gaussian white noises with different signal-to-noise ratios (SNRs). The Salinas dataset and the Avon dataset are selected in this experiment. δ is set to the maximum value of the RMSEs between all pixels in a small homogeneous region. Specifically, δ is set to 0.01 and 0.017 for the Salinas dataset and the Avon dataset, respectively. For the Salinas dataset, each target has a size of 11×11 pixels, and thus, the inner window size should be set at least 23×23 to exclude target pixels from the local background during the sliding process [37]. Therefore, the dual window size is set to (15, 25), (19, 25), and (23, 25), generating a highly contaminated, a slightly contaminated, and a pure background dictionary, respectively. The maximum size of targets in the Avon dataset is known as 8×8 pixels. However,

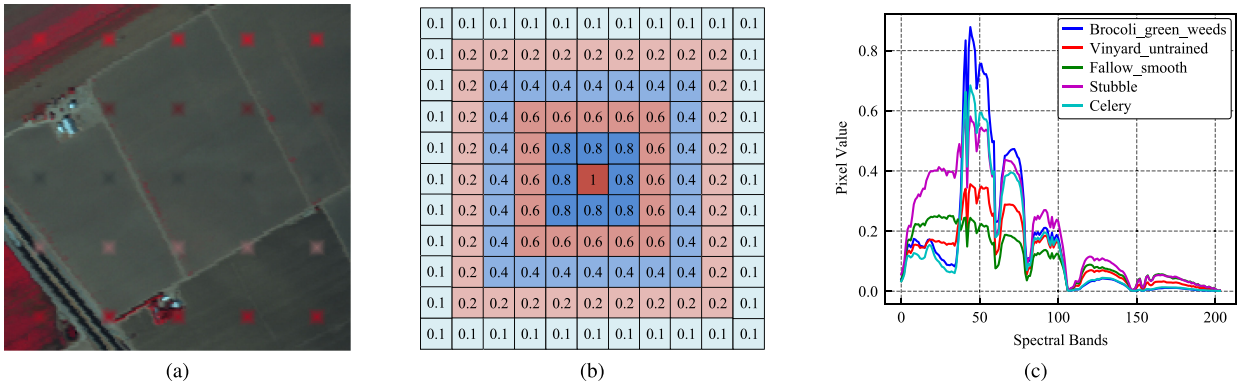

Fig. 2. Simulated Salinas dataset. (a) False color image. (b) Abundance map of each target. (c) Prior target dictionary.

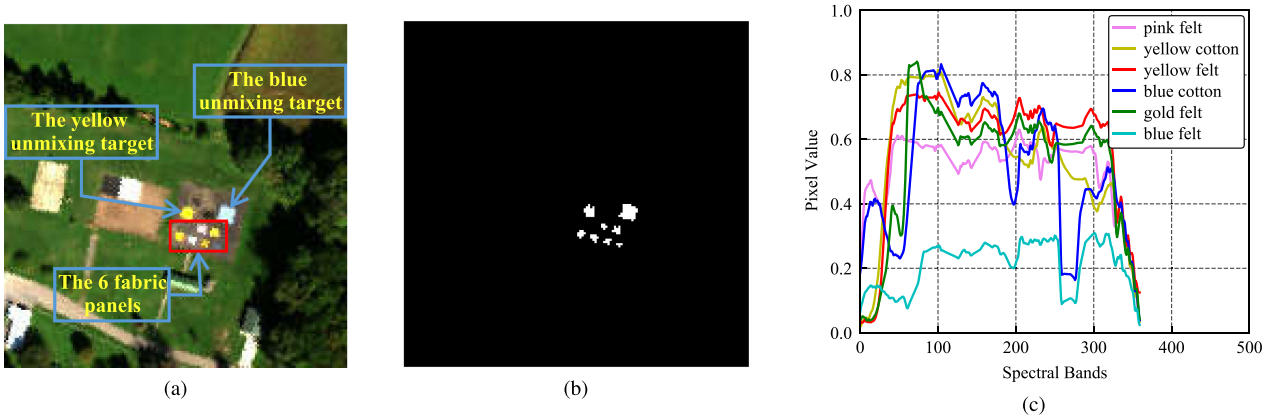

Fig. 3. Real Avon dataset. (a) False color image. (b) Ground truth map. (c) Prior target dictionary.

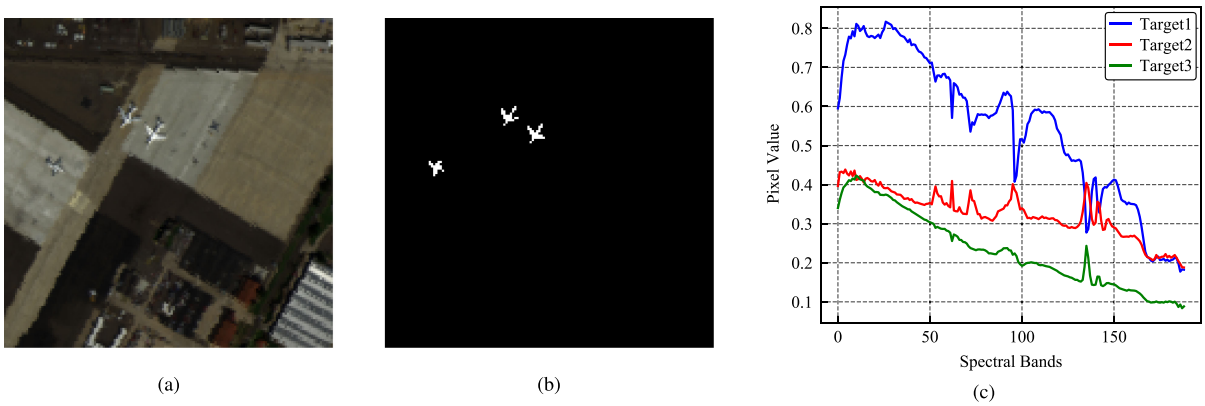

Fig. 4. Real SanDiego dataset. (a) False color image. (b) Ground truth map. (c) Prior target dictionary.

since the targets in this dataset are densely distributed, it is difficult to set a proper inner window size to exclude target pixels from the local background. Consequently, the dual window size is set to (9, 19), (11, 19), and (13, 19), generating a background dictionary with different target contamination levels. The SNR varies from 10 to 40 dB.

First, we investigate the robustness of detection performance to noises and target contamination. The commonly used receiver operating characteristic (ROC) curve [38] and the area under the ROC curve (AUC) are used for detection performance evaluation. The AUC values achieved by our ICSR method on the Salinas and Avon datasets with different SNRs are shown in Fig. 5(a) and (b), respectively. It can be clearly observed that if the SNR is smaller than 25 dB, the AUC values improve rapidly. That is because if the SNR is too small, the spectral variabilities between pixels are very large. Thus, the target

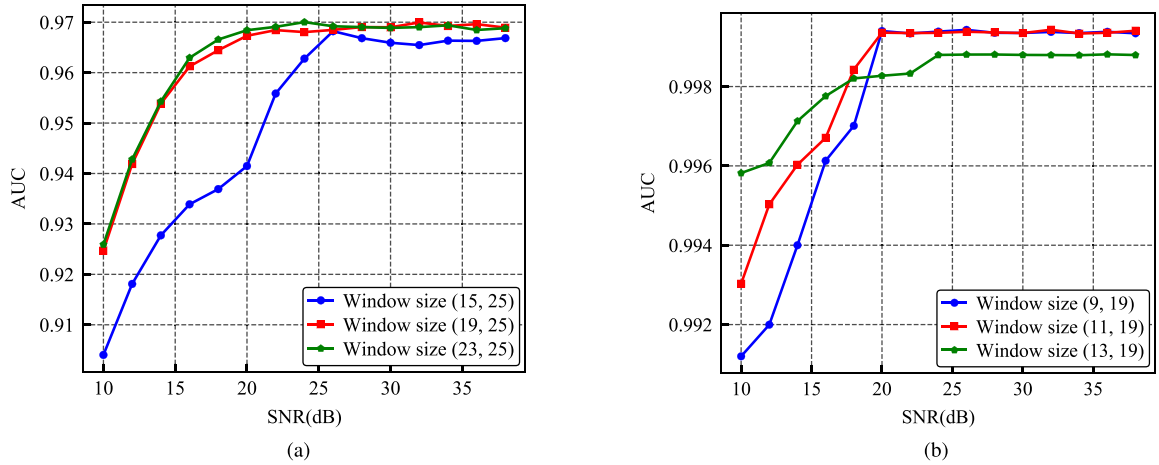

Fig. 5. AUC values achieved on the two datasets with different values of parameter δ. (a) Salinas dataset. (b) Avon dataset.

TABLE I
TARGET ABUNDANCES RECOVERED BY ICSR ON THE SALINAS DATASET WITH DIFFERENT SNRS

True Abundances		1.0	0.8	0.6	0.4	0.2	0.1
SNR=10	Mean	0.9985	0.7869	0.5702	0.3550	0.1359	0.0510
	STD	0.0028	0.0306	0.0651	0.0756	0.0739	0.0616
	RE	0.15%	1.63%	4.97%	11.24%	32.04%	49.03%
SNR=20	Mean	0.9992	0.8019	0.6056	0.4031	0.1955	0.1048
	STD	0.0011	0.0336	0.0636	0.0905	0.1185	0.1211
	RE	0.08%	0.23%	0.93%	0.76%	2.26%	4.78%
SNR=30	Mean	0.9994	0.8004	0.6079	0.4064	0.2021	0.1062
	STD	0.0010	0.0311	0.0656	0.0926	0.1198	0.1234
	RE	0.06%	0.05%	1.31%	1.60%	1.07%	6.22%
SNR=40	Mean	0.9994	0.8014	0.6063	0.4064	0.2030	0.1060
	STD	0.0010	0.0310	0.0637	0.0942	0.1207	0.1235
	RE	0.06%	0.17%	1.04%	1.61%	1.52%	5.99%

pixels are not effectively unmixed, especially for the subpixel targets with small abundances, resulting in missing alarms. If the SNR is larger than 25 dB, the AUC values remain largely the same. It shows the detection robustness of our ICSR method to small noises. When the SNR is larger than 25 dB, the AUC value differences between these three window sizes are very small. It demonstrates that our ICSR method is robust to target contamination. Note that the AUC value achieved on the Avon dataset with window size (13, 19) is smaller than that of window size (9, 19) and window size (11, 19). That is because the background endmember of the subpixel target is more similar to the pixel in its neighborhood. Therefore, the larger the inner window size is, the more inaccurate the extracted background endmember is, resulting in a degenerated detection performance. In summary, our ICSR method exhibits a relatively stronger detection robustness to noises and target contamination.

Second, we investigate the robustness of unmixing performance to noises and target contamination. The mean and standard deviation (STD) of the recovered target abundances (with the same true abundance) are adopted for unmixing performance evaluation. Meanwhile, the relative error (RE) of target abundance is also adopted; it is defined as

$$\mathrm{RE} = |T - \mu|/T \times 100\% \tag{16}$$

where T denotes the true target abundance and μ denotes the mean of the recovered target abundances.

To avoid edge effects, for the real Avon dataset, the mean, STD, and RE are calculated based on a smaller subset using pixels with two guard pixels on all sides of the target. These three evaluation indexes achieved on the Salinas dataset with different SNRs and on the Avon dataset with different window sizes are reported in Tables I and II, respectively. From Table I, it can be clearly observed that the mean of the recovered target abundances is very close to the ground truth with a low STD. The mean, STD, and RE results achieved with the SNR equal to 20, 30, and 40 dB are very similar. When the SNR is equal to 10 dB, the unmixing errors are enlarged especially for the subpixel targets with small abundances. It demonstrates the unmixing robustness of our ICSR method to small noises. From Table II, comparing these three evaluation indexes with different window sizes, we can see that the unmixing performance does not degenerate. This clearly demonstrates that ICSR can

TABLE II
TARGET ABUNDANCES RECOVERED BY ICSR ON THE AVON DATASET WITH DIFFERENT WINDOW SIZES

Materials		yellow felt	yellow cotton	blue cotton	blue felt
True Abundances		0.75	0.25	0.5	0.5
Window Size (7, 19)	Mean	0.7128	0.2486	0.4928	0.4723
	STD	0.0851	0.0442	0.0098	0.0263
	RE	4.96%	0.56%	1.43%	5.54%
Window Size (9, 19)	Mean	0.7136	0.2527	0.4930	0.4772
	STD	0.0838	0.0506	0.0098	0.0256
	RE	4.86%	1.06%	1.40%	4.56%
Window Size (11, 19)	Mean	0.7136	0.2527	0.4942	0.4780
	STD	0.0838	0.0506	0.0095	0.0259
	RE	4.86%	1.06%	1.15%	4.41%
Window Size (13, 19)	Mean	0.7136	0.2527	0.4938	0.4815
	STD	0.0838	0.0506	0.0093	0.0220
	RE	4.86%	1.06%	1.25%	3.70%

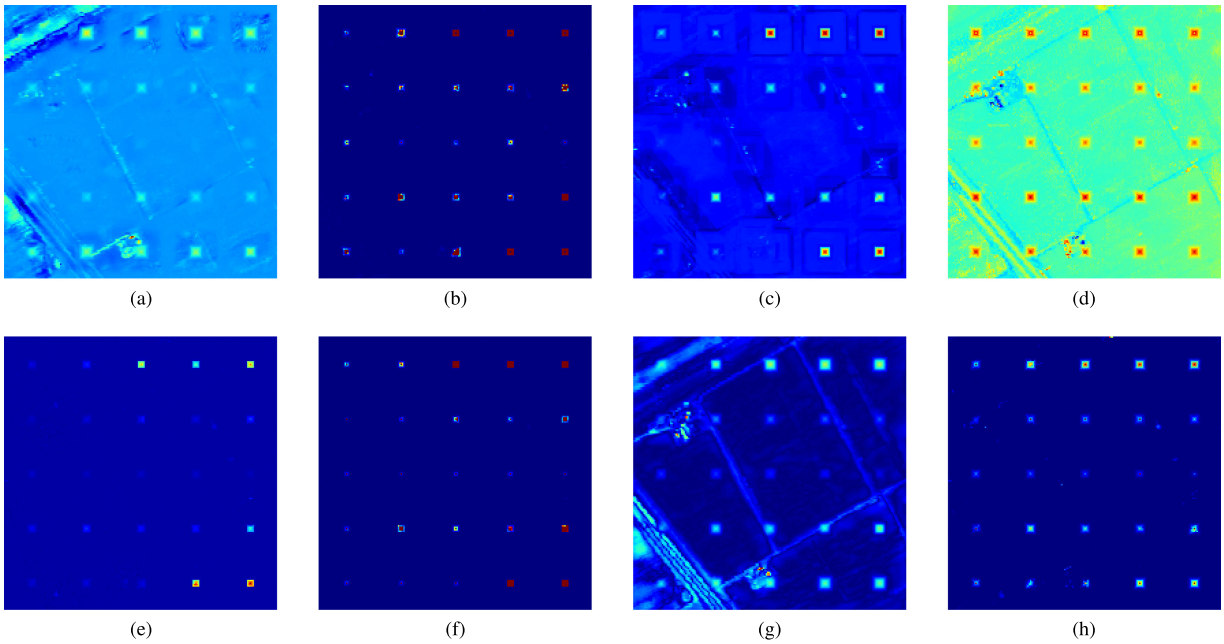

Fig. 6. Detection maps achieved on the Salinas dataset with window size (15, 25). (a) SMF. (b) MSD. (c) SVM. (d) SR. (e) SRBBH. (f) HSS. (g) DM-BDL. (h) ICSR.

accurately recover target abundance even if the target signals are blended into the local background. In summary, our ICSR method exhibits a relatively stronger unmixing robustness to noises and target contamination.

C. Detection Performance Evaluation

The proposed ICSR algorithm is compared to several aforementioned detectors, including SMF [10], MSD [12], SVM (described in Section II-A), SR (described in Section II-B), SRBBH [18], HSS [19], and DM-BDL [4]. Among them, DM-BDL is a global method, and there is no need to set window sizes. The prior target spectrum for SMF is the mean of the target atoms in $\boldsymbol{A}_t$. $\boldsymbol{A}_t$ and $\boldsymbol{A}_b$ are used to generate the target and background subspaces for MSD [39], respectively. All parameters of these detectors are empirically tuned to their optimum. For the Salinas dataset, the dual window size is set to (15, 25), (19, 25) and (23, 25), resulting in 400, 264, and 96 training samples in the background dictionary. For the Avon dataset, the dual window size is set to (9, 19), (11, 19), and (13, 19), resulting in 280, 240, and 192 training samples in the background dictionary. Therefore, the local background dictionary is contaminated by target pixels with different levels as mentioned above.

The detection maps achieved on the Salinas dataset with window size (15, 25) are shown in Fig. 6, achieved on the Avon dataset with window size (9, 19) are shown in Fig. 7, and

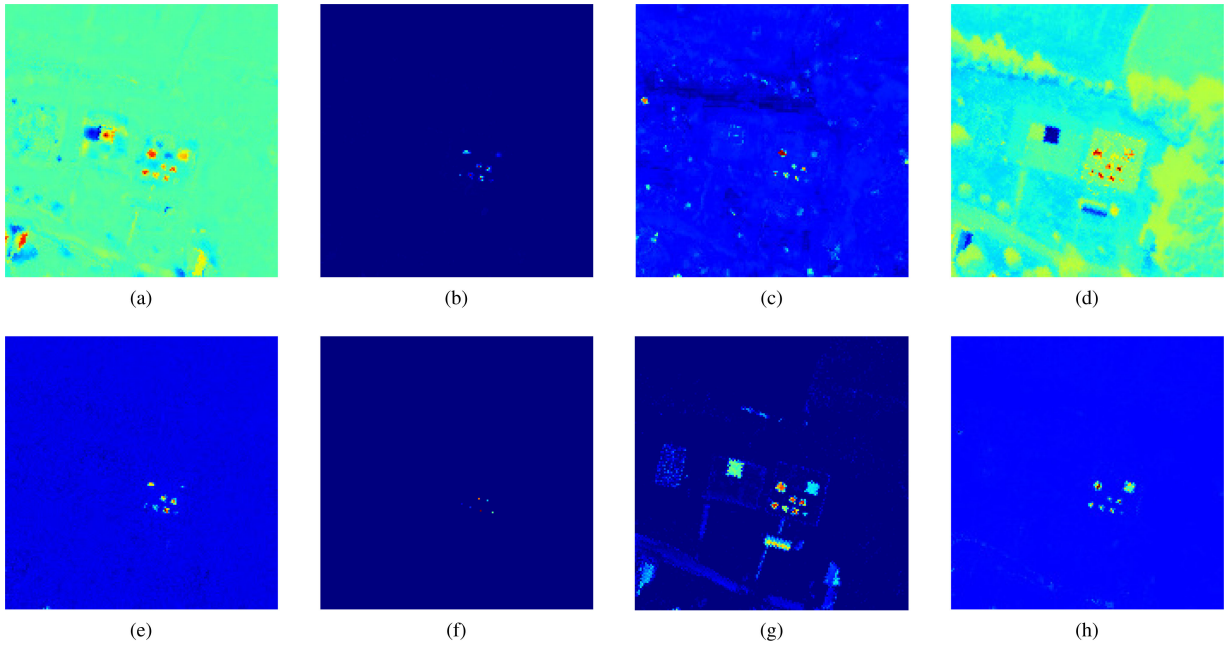

Fig. 7. Detection maps achieved on the Avon dataset with window size (9, 19). (a) SMF. (b) MSD. (c) SVM. (d) SR. (e) SRBBH. (f) HSS. (g) DM-BDL. (h) ICSR.

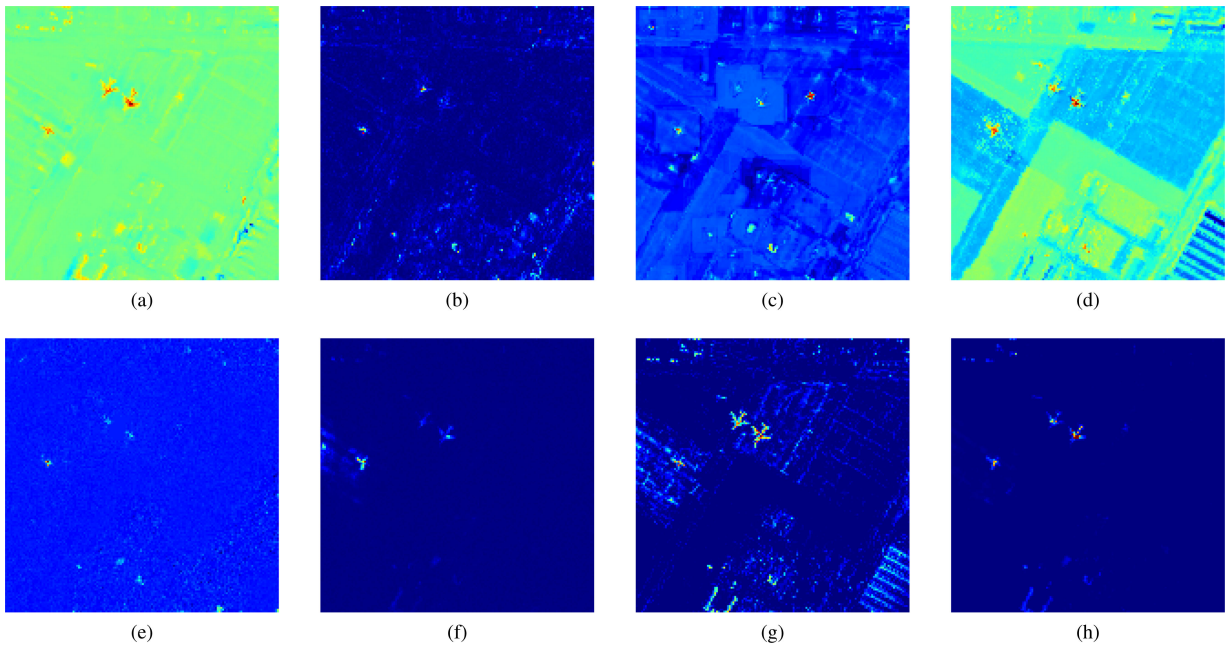

Fig. 8. Detection maps achieved on the SanDiego dataset with window size (9, 19) (a) SMF. (b) MSD. (c) SVM. (d) SR. (e) SRBBH. (f) HSS. (g) DM-BDL. (h) ICSR.

achieved on the SanDiego dataset with window size (9, 19) are shown in Fig. 8. It can be seen that there exists more noisy pixels in the detection map of SMF than other algorithms, resulting in a lower detection probabilities. Although MSD achieves a promising background suppression performance, most target pixels are darker than other methods. The SVM achieves a promising target enhancement results when the target abundance is large. However, when the target abundance is small, the detection values of these target pixels are very small. DM-BDL, as a global method, remains more edge textures. As compared to SR, the background pixels of our ICSR method are more dark, which indicates that the ICSR method achieves a better background suppression. Compared with SRBBH and HSS, the target pixels of our ICSR method are more obvious, especially when

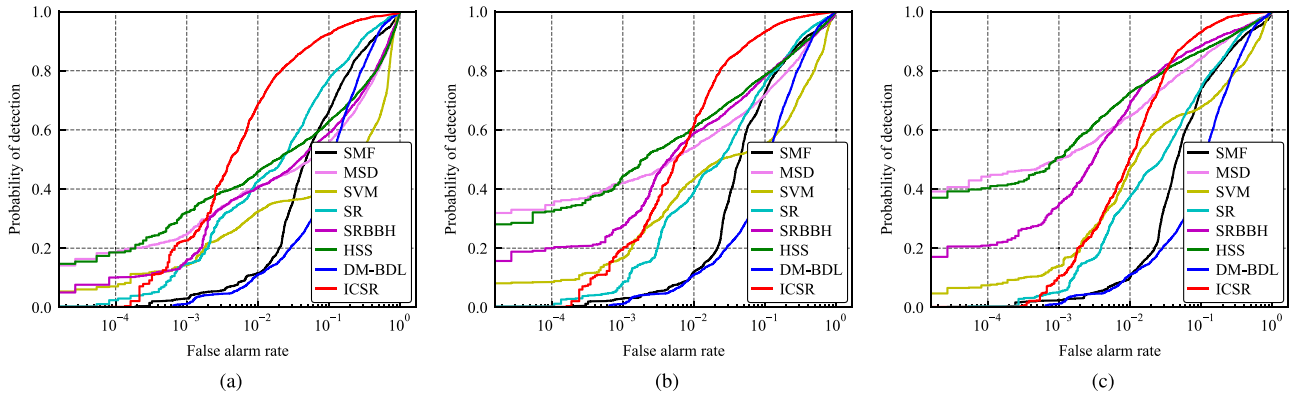

Fig. 9. ROC curves achieved on the Salinas dataset with different dual window sizes. (a) Dual window size (15, 25). (b) Dual window size (19, 25). (c) Dual window size (23, 25).

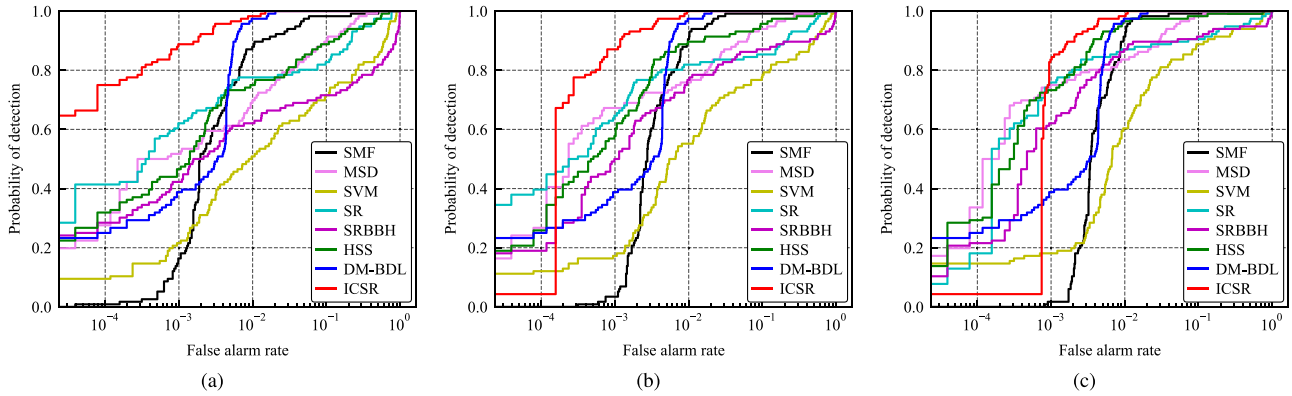

Fig. 10. ROC curves achieved on the Avon dataset with different dual window sizes. (a) Dual window size (9, 19). (b) Dual window size (11, 19). (c) Dual window size (13, 19).

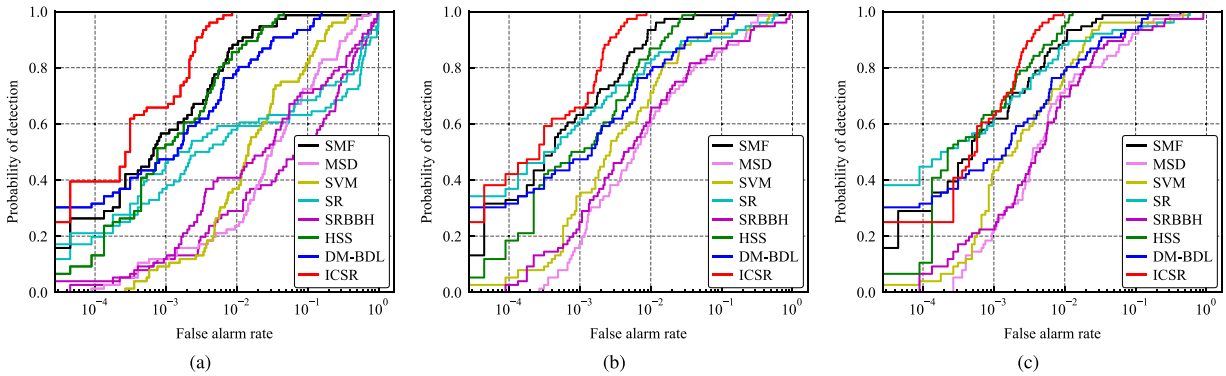

Fig. 11. ROC curves achieved on the SanDiego dataset with different dual window sizes. (a) Dual window size (9, 19). (b) Dual window size (13, 19). (c) Dual window size (17, 19).

the target abundance is small. This indicates that the proposed ICSR method achieves a better target enhancement. In summary, the proposed ICSR method has achieved the best performance when both background suppression and target enhancement are considered.

The ROC curves achieved on these three datasets with different dual window sizes are shown in Figs. 9–11, and the AUC values are reported in Tables III –V. We describe the superiority of our ICSR algorithm on the Avon dataset for simplification. As shown in Fig. 10(a), if the window size is set to (9, 19), ICSR achieves the highest detection probability at all false alarm rates. Moreover, the AUC performance achieved by ICSR outperforms other detectors by a large margin. As shown in Fig. 10(b), if the window size is set to (11, 19), SR achieves the best ROC

TABLE III
AUC (IN PERCENT) VALUES ACHIEVED ON THE SALINAS DATASET

Window Size	SMF	MSD	SVM	SR	SRBBH	HSS	DM-BDL	ICSR
(15, 25)	86.14	77.85	66.57	90.69	79.73	80.16	82.47	**96.58**
(19, 25)	87.62	87.96	78.70	90.33	89.62	90.13	82.47	**96.98**
(23, 25)	87.51	93.32	84.30	90.00	94.17	93.75	82.47	**96.88**

TABLE IV
AUC (IN PERCENT) VALUES ACHIEVED ON THE AVON DATASET

Window Size	SMF	MSD	SVM	SR	SRBBH	HSS	DM-BDL	ICSR
(9, 19)	98.81	96.79	85.39	94.21	81.19	95.62	99.68	**99.93**
(11, 19)	99.08	97.86	88.81	94.63	90.73	98.02	99.68	**99.94**
(13, 19)	98.84	99.10	93.42	95.67	94.32	99.07	99.68	**99.88**

TABLE V
AUC (IN PERCENT) VALUES ACHIEVED ON THE SANDIEGO DATASET

Window Size	SMF	MSD	SVM	SR	SRBBH	HSS	DM-BDL	ICSR
(9, 19)	98.62	89.77	94.82	81.90	84.91	99.48	98.55	**99.90**
(13, 19)	98.69	95.41	96.26	96.31	93.14	99.53	98.55	**99.90**
(17, 19)	99.13	97.20	97.73	97.38	95.81	99.81	98.55	**99.88**

performance when the false alarm rate is lower than 10^{-4}. In contrast, ICSR achieves the highest detection probability when the false alarm rate is higher than 10^{-4}. With respect to the whole range of false alarm rate, the AUC value achieved by ICSR is 5.31% higher than that of SR. Similarly, as shown in Fig. 10(c), if the window size is set to (13, 19), ICSR achieves the best ROC performance if the false alarm rate is higher than 10^{-3} and achieves the highest AUC values. Note that the proposed method significantly improves the detection performance on these two datasets. Specifically, the AUC value achieved by ICSR can reach 99.88%, which is 4.21% higher than SR and 5.56% higher than SRBBH, respectively. Comparing the ROC curves and AUC values obtained with different window sizes, it can be observed that all local methods except ICSR and SMF degenerate rapidly when the inner window size is decreased. This clearly validates the effectiveness of ICSR in suppressing target signals in the local background. Similar conclusions can be drawn on the Salinas dataset and the SanDiego dataset. Note that the detection performance of SMF is improved when the inner window size is decreased. That is because the accuracy of the estimated background covariance matrix increases with the number of background training samples. In summary, the proposed ICSR method achieves the best detection performance as compared to other traditional detectors.

D. Unmixing Performance Evaluation

In the previous experiment for detection performance evaluation, the subpixel targets are unmixed simultaneously by our ICSR algorithm. The abundance maps of different targets obtained by ICSR on the Salinas dataset are presented in Fig. 12, where the window size is set to (15, 25). The abundance maps of different targets obtained by ICSR on the Avon dataset are presented in Fig. 13, where the window size is set to (9, 19). From Fig. 13(a) and (e), it can be seen that the abundance maps of pink felt and gold felt only have high values in their corresponding target panels. From Fig. 12(a)–(e), it can be seen that the five target materials have achieved accurate abundances, and the background regions have low abundances. From Fig. 13(b)–(d) and (f), it can be seen that the four target materials (i.e., yellow cotton, yellow felt, blue cotton, and blue felt) have achieved accurate abundances. It should be noticed that the abundance map of blue felt has some noisy pixels in the edges. That is because the spectrum of the edge between grass and asphalt is similar to the spectrum of blue felt. To sum up, the proposed ICSR method provides satisfactory unmixing results in terms of the accurate abundance estimation for the target pixels that exist in the image. This accurate target abundance estimation also improves the detection performance.

Furthermore, the proposed ICSR algorithm is compared to several classical unmixing methods, including FCLSU [40], CLSU [40], SUnSAL [41], NCM [42], and ALMM [7]. First, the vertex component analysis [43] method was applied to extracting 8 and 12 background endmembers for the Salinas dataset and the Avon dataset, respectively. Second, the endmember dictionary for these unmixing methods is combined by the background endmembers and prior target dictionary. Finally, these unmixing methods are applied with this endmember dictionary. Note that our ICSR method only uses the prior target dictionary as the endmember dictionary. These three evaluation indexes achieved on the Salinas dataset and the Avon dataset are reported in Tables VI and VII, respectively. It can be clearly observed that the mean of the recovered target abundances achieved by our ICSR method is very close to the ground truth with a low STD. For the Salinas dataset, the RE achieved by ICSR is lower than 2% in most situations, especially for the pixels with large target abundances. For the Avon dataset, the RE achieved by ICSR is lower than 5%. Compared to FCLSU, CLSU, SUnSAL, NCM, and ALMM, our

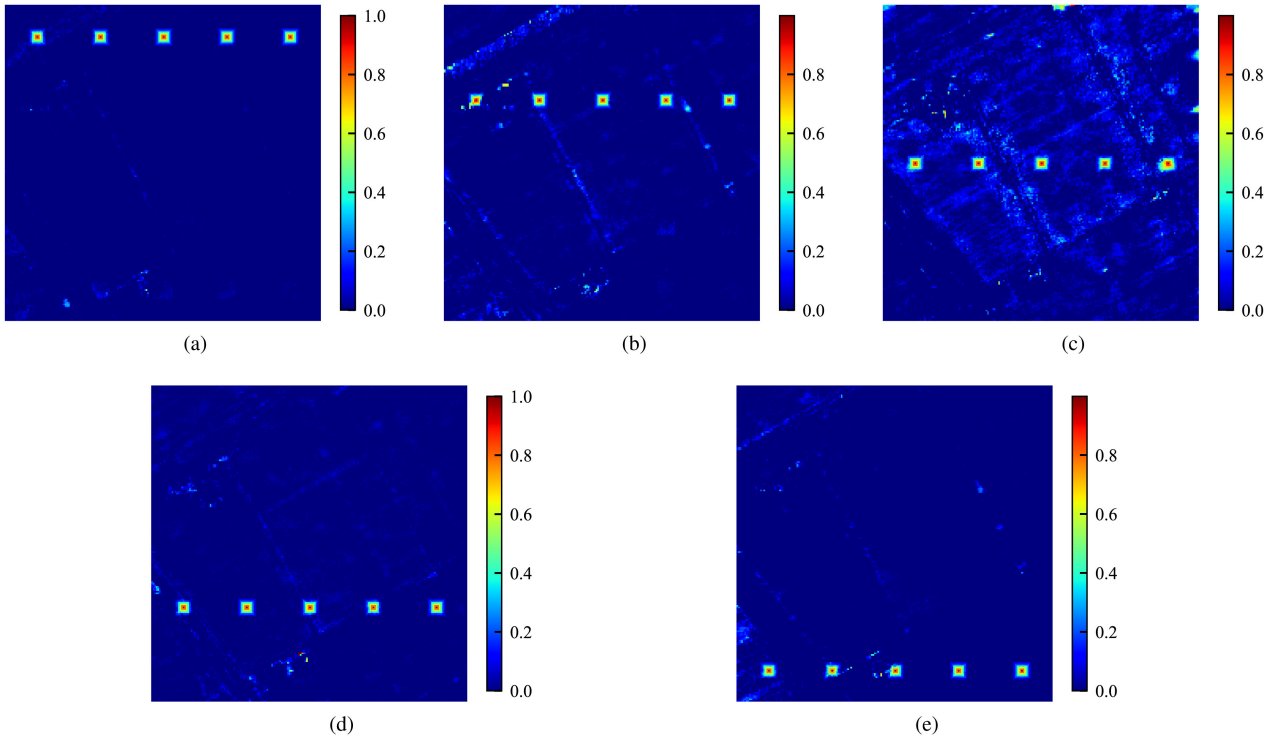

Fig. 12. Abundance maps of different targets achieved by ICSR on the Salinas dataset with window size (15, 19). (a) Brocoli-green-weeds. (b) Vinyard-untrained. (c) Fallow-smooth. (d) Stubble. (e) Celery.

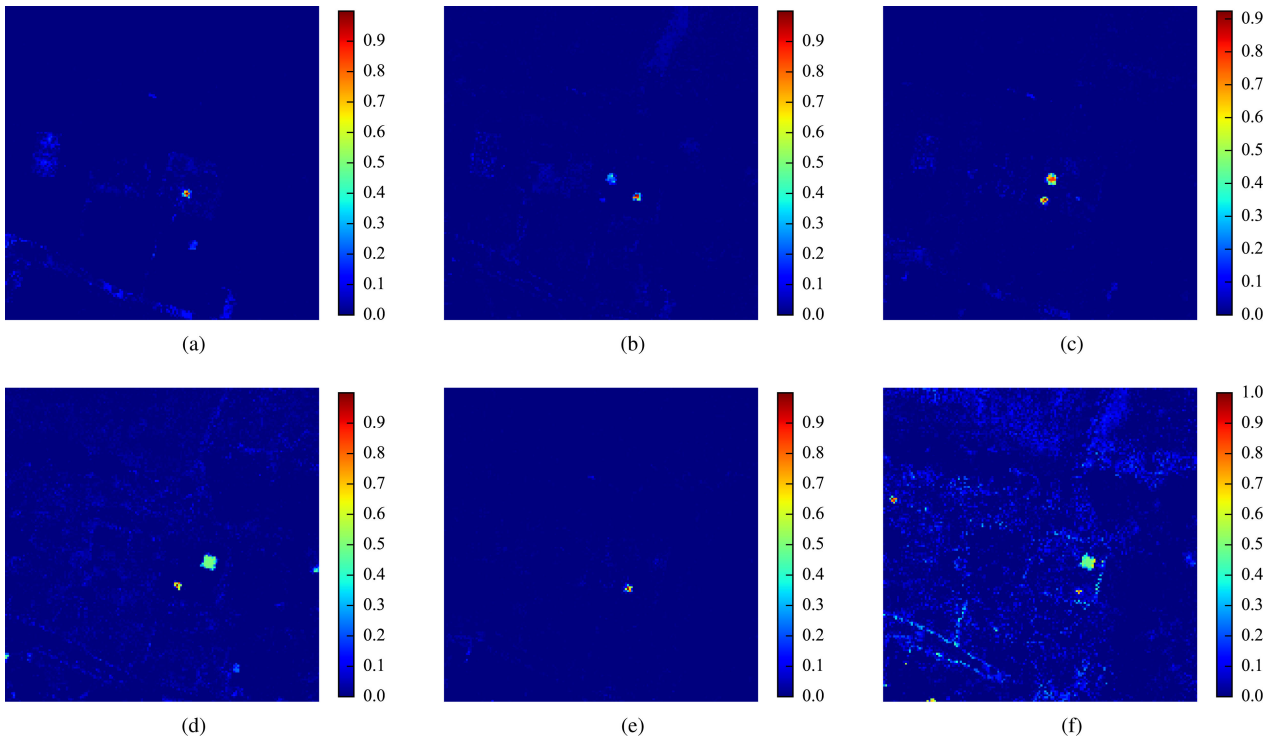

Fig. 13. Abundance maps of different targets achieved by ICSR on the Avon dataset with window size (9, 19). (a) Pink felt. (b) Yellow cotton. (c) Yellow felt. (d) Blue cotton. (e) Gold felt. (f) Blue felt.

TABLE VI
TARGET ABUNDANCES RECOVERED BY DIFFERENT METHODS ON THE SALINAS DATASET

True Abundances		1.0	0.8	0.6	0.4	0.2	0.1
FCLSU	Mean	1.0000	0.8017	0.6031	0.4000	0.2378	0.1897
	STD	0.0000	0.0899	0.1769	0.2633	0.3154	0.3279
	RE	0.00%	0.22%	0.52%	0.00%	18.91%	89.71%
CLSU	Mean	1.0000	0.8024	0.6047	0.4012	0.2439	0.1976
	STD	0.0000	0.0949	0.1866	0.2782	0.3315	0.3471
	RE	0.00%	0.30%	0.79%	0.31%	21.94%	97.63%
SUnSAL	Mean	1.0000	0.7872	0.5774	0.3613	0.2281	0.1979
	STD	0.0000	0.1054	0.2068	0.3092	0.3496	0.3583
	RE	0.00%	1.59%	3.77%	9.67%	14.03%	97.86%
NCM	Mean	0.4037	0.3777	0.3418	0.2344	0.1392	0.1186
	STD	0.1738	0.1581	0.1727	0.1746	0.1632	0.1507
	RE	59.63%	52.79%	43.04%	41.39%	30.40%	18.59%
ALMM	Mean	0.9600	0.7842	0.5916	0.3315	0.0699	0.0214
	STD	0.0260	0.1276	0.1988	0.2157	0.1103	0.0601
	RE	4.00%	1.98%	1.39%	17.13%	65.07%	78.63%
ICSR	Mean	0.9994	0.8014	0.6063	0.4064	0.2030	0.1060
	STD	0.0010	0.0310	0.0637	0.0942	0.1207	0.1235
	RE	0.06%	0.17%	1.04%	1.61%	1.52%	5.99%

TABLE VII
TARGET ABUNDANCES RECOVERED BY DIFFERENT METHODS ON THE AVON DATASET

Materials		yellow felt	yellow cotton	blue cotton	blue felt
True Abundances		0.75	0.25	0.5	0.5
FCLSU	Mean	0.7057	0.1377	0.4837	0.4264
	STD	0.0463	0.0732	0.0109	0.0326
	RE	5.90%	44.91%	3.27%	14.72%
CLSU	Mean	0.7045	0.1321	0.4828	0.4245
	STD	0.0455	0.0726	0.0107	0.0324
	RE	6.06%	47.17%	3.44%	15.11%
SUnSAL	Mean	0.6969	0.1442	0.4783	0.5210
	STD	0.0397	0.0671	0.0098	0.0208
	RE	7.08%	42.31%	4.35%	4.20%
NCM	Mean	0.2482	0.0939	0.3749	0.0619
	STD	0.1452	0.0530	0.0556	0.0580
	RE	66.91%	62.45%	25.02%	87.62%
ALMM	Mean	0.1833	0.0281	0.3597	0.2680
	STD	0.1518	0.0391	0.0379	0.0399
	RE	75.55%	88.77%	28.07%	46.41%
ICSR	Mean	0.7136	0.2527	0.4938	0.4815
	STD	0.0838	0.0506	0.0093	0.0220
	RE	4.86%	1.06%	1.25%	3.70%

ICSR method achieves more accurate abundances, especially for targets with small abundances. Meanwhile, ICSR has a lower STD and a lower RE. Comparing these three evaluation indexes achieved on the two datasets, it can be seen that our ICSR method achieves the best unmixing performance. In summary, the proposed ICSR algorithm has achieved a promising performance in terms of target abundance recovery. This promising target abundance recovery is the guarantee of excellent target detection performance.

E. Running Time

In this section, we investigate the running time of the aforementioned algorithms. The running time consumed by different algorithms on the two datasets is reported in Table VIII. All algorithms were implemented in Python 3.5 on a desktop computer equipped with an Intel Core i7-3770 CPU (at 3.4 GHz) and a 8 GB of RAM memory. Moreover, the SMO method is implemented in C++ and encapsulated into a pyd extension module that can be called by python interpreter.

TABLE VIII
RUNNING TIMES (IN SECONDS) ACHIEVED ON THE TWO DATASETS

Datasets	Window Sizes	SMF	MSD	SVM	SR	SRBBH	HSS	DM-BDL	ICSR
Salinas Dataset	(15, 25)	734.1	762.8	84.4	111.7	203.6	207.1	**12.6**	196.6
	(19, 25)	730.2	742.9	61.1	108.1	196.9	199.2	**12.6**	147.0
	(23, 25)	675.0	714.7	34.6	103.9	190.0	194.4	**12.6**	86.2
Avon Dataset	(9, 19)	833.5	940.2	65.1	77.6	101.4	107.8	**8.4**	116.3
	(11, 19)	809.5	956.9	57.1	78.9	101.7	100.7	**8.4**	103.4
	(13, 19)	853.5	828.7	47.0	72.0	93.1	92.3	**8.4**	87.2
SanDiego Dataset	(9, 19)	377.5	390.0	31.0	32.9	54.6	113.0	**8.90**	58.2
	(13, 19)	366.6	394.6	24.5	31.2	53.0	111.3	**8.90**	48.0
	(17, 19)	364.5	381.9	19.9	30.6	52.1	112.4	**8.90**	39.9

The inverse operation and eigenvalue decomposition used in the aforementioned methods are calculated by the high-performance LAPACK-library-based scipy functions. Therefore, the running time of these methods is relatively fast. It can be seen that the global method DM-BDL runs fastest, and its running time is not related to the window sizes. Our ICSR method is slightly slower than SVM and SR and comparable to SRBBH and HSS. However, the proposed ICSR method is faster than SMF and MSD by a large margin. Specifically, the running time of our ICSR is about 1/7 of that of SMF and MSD. In summary, the proposed ICSR method has a relatively lower running time.

V. CONCLUSION

In this article, we propose a novel algorithm named ICSR to detect and unmix subpixel target simultaneously. In the proposed model, the prior target spectra are considered as target endmembers, while the background endmembers are extracted from the local background by an iterative process. With the sum-to-one and nonnegativity constraints on representation coefficients, each test pixel is separately represented by the background endmembers and the union of background and target endmembers. Note that this algorithm can detect subpixel target and obtain its target abundance, even if the local background is contaminated by target signals. Experimental results on both synthetic and real HSI datasets demonstrate the superiority of the proposed algorithm in both detection performance and unmixing performance. Meanwhile, the proposed algorithm also has a relatively lower running time. Most importantly, this method has a great potential in practical applications of hyperspectral remote sensing.

REFERENCES

[1] M. Borengasser, W. S. Hungate, and R. Watkins, *Hyperspectral Remote Sensing—Principles and Applications*. Boca Raton, FL, USA: CRC Press, 2008.

[2] X. Cao, X. Fu, C. Xu, and D. Meng, "Deep spatial-spectral global reasoning network for hyperspectral image denoising," *IEEE Trans. Geosci. Remote Sens.*, vol. 60, 2022, Art no. 5504714.

[3] L. Gao, D. Hong, J. Yao, B. Zhang, P. Gamba, and J. Chanussot, "Spectral superresolution of multispectral imagery with joint sparse and low-rank learning," *IEEE Trans. Geosci. Remote Sens.*, vol. 59, no. 3, pp. 2269–2280, Mar. 2021.

[4] T. Cheng and B. Wang, "Decomposition model with background dictionary learning for hyperspectral target detection," *IEEE J. Sel. Topics Appl. Earth Observ. Remote Sens.*, vol. 14, pp. 1872–1884, Jan. 2021.

[5] Q. Ling, Y. Guo, Z. Lin, L. Liu, and W. An, "A constrained sparse representation-based binary hypothesis model for target detection in hyperspectral imagery," *IEEE J. Sel. Topics Appl. Earth Observ. Remote Sens.*, vol. 12, no. 6, pp. 1933–1947, Jun. 2019.

[6] D. Hong *et al.*, "Endmember-guided unmixing network (EGU-Net): A general deep learning framework for self-supervised hyperspectral unmixing," *IEEE Trans. Neural Netw. Learn. Syst.*, pp. 1–14, May 28 2021, doi: 10.1109/TNNLS.2021.3082289.

[7] D. Hong, N. Yokoya, J. Chanussot, and X. X. Zhu, "An augmented linear mixing model to address spectral variability for hyperspectral unmixing," *IEEE Trans. Image Process.*, vol. 28, no. 4, pp. 1923–1938, Apr. 2019.

[8] J. Yao, D. Meng, Q. Zhao, W. Cao, and Z. Xu, "Nonconvex-sparsity and nonlocal-smoothness-based blind hyperspectral unmixing," *IEEE Trans. Image Process.*, vol. 28, no. 6, pp. 2991–3006, Jun. 2019.

[9] D. Hong, N. Yokoya, J. Chanussot, J. Xu, and X. X. Zhu, "Joint and progressive subspace analysis (JPSA) with spatial-spectral manifold alignment for semisupervised hyperspectral dimensionality reduction," *IEEE Trans. Cybern.*, vol. 51, no. 7, pp. 3602–3615, Jul. 2021.

[10] N. M. Nasrabadi, "Regularized spectral matched filter for target recognition in hyperspectral imagery," *IEEE Signal Process. Lett.*, vol. 15, no. 3, pp. 317–320, Mar. 2008.

[11] S. Kraut, L. L. Scharf, and L. T. McWhorter, "Adaptive subspace detectors," *IEEE Trans. Signal Process.*, vol. 49, no. 1, pp. 1–16, Jan. 2001.

[12] L. L. Scharf and B. Friedlander, "Matched subspace detectors," *IEEE Trans. Signal Process.*, vol. 42, no. 8, pp. 2146–2157, Aug. 1994.

[13] N. M. Nasrabadi, "Hyperspectral target detection: An overview of current and future challenges," *IEEE Signal Process. Mag.*, vol. 31, no. 1, pp. 34–44, Jan. 2014.

[14] B. Demir and S. Ertürk, "Empirical mode decomposition of hyperspectral images for support vector machine classification," *IEEE Trans. Geosci. Remote Sens.*, vol. 48, no. 11, pp. 4071–4084, Nov. 2010.

[15] Y. Dong, B. Du, L. Zhang, and X. Hu, "Hyperspectral target detection via adaptive information-theoretic metric learning with local constraints," *Remote Sens.*, vol. 10, no. 9, Sep. 2018, Art. no. 1415.

[16] Y. Zhang, K. Wu, B. Du, L. Zhang, and X. Hu, "Hyperspectral target detection via adaptive joint sparse representation and multi-task learning with locality information," *Remote Sens.*, vol. 9, no. 5, May 2017, Art. no. 482.

[17] Y. Chen, N. M. Nasrabadi, and T. D. Tran, "Sparse representation for target detection in hyperspectral imagery," *IEEE J. Sel. Topics Signal Process.*, vol. 5, no. 3, pp. 629–640, Jun. 2011.

[18] Y. Zhang, B. Du, and L. Zhang, "A sparse representation-based binary hypothesis model for target detection in hyperspectral images," *IEEE Trans. Geosci. Remote Sens.*, vol. 53, no. 3, pp. 1346–1354, Mar. 2015.

[19] B. Du, Y. Zhang, L. Zhang, and D. Tao, "Beyond the sparsity-based target detector: A hybrid sparsity and statistics based detector for hyperspectral images," *IEEE Trans. Image Process.*, vol. 25, no. 11, pp. 5345–5357, Nov. 2016.

[20] N. Keshava and J. F. Mustard, "Spectral unmixing," *IEEE Signal Process. Mag.*, vol. 19, no. 1, pp. 44–57, Jan. 2002.

[21] S. Zhang, J. Li, H.-C. Li, C. Deng, and A. Plaza, "Spectral-spatial weighted sparse regression for hyperspectral image unmixing," *IEEE Trans. Geosci. Remote Sens.*, vol. 56, no. 6, pp. 3265–3276, Jun. 2018.

[22] L. Miao and H. Qi, "Endmember extraction from highly mixed data using minimum volume constrained nonnegative matrix factorization," *IEEE Trans. Geosci. Remote Sens.*, vol. 45, no. 3, pp. 765–777, Mar. 2007.

[23] X. Wang, Y. Zhong, L. Zhang, and Y. Xu, "Spatial group sparsity regularized nonnegative matrix factorization for hyperspectral unmixing," *IEEE Trans. Geosci. Remote Sens.*, vol. 55, no. 11, pp. 6287–6304, Nov. 2017.

[24] Y. Su, J. Li, A. Plaza, A. Marinoni, P. Gamba, and S. Chakravortty, "DAEN: Deep autoencoder networks for hyperspectral unmixing," *IEEE Trans. Geosci. Remote Sens.*, vol. 57, no. 7, pp. 4309–4321, Jul. 2019.
[25] B. Palsson, M. O. Ulfarsson, and J. R. Sveinsson, "Convolutional autoencoder for spectral–spatial hyperspectral unmixing," *IEEE Trans. Geosci. Remote Sens.*, vol. 59, no. 1, pp. 535–549, Jan. 2021.
[26] M.-D. Iordache, J. M. Bioucas-Dias, and A. Plaza, "Total variation spatial regularization for sparse hyperspectral unmixing," *IEEE Trans. Geosci. Remote Sens.*, vol. 50, no. 11, pp. 4484–4502, Nov. 2012.
[27] S. Zhang, J. Li, K. Liu, C. Deng, L. Liu, and A. Plaza, "Hyperspectral unmixing based on local collaborative sparse regression," *IEEE Geosci. Remote Sens. Lett.*, vol. 13, no. 5, pp. 631–635, May 2016.
[28] J. Liu and J. Zhang, "Spectral unmixing via compressive sensing," *IEEE Trans. Geosci. Remote Sens.*, vol. 52, no. 11, pp. 7099–7110, Nov. 2014.
[29] C. Cortes and V. Vapnik, "Support vector network," *Mach. Learn.*, vol. 20, no. 3, pp. 273–297, 1995.
[30] R.-E. Fan, P.-H. Chen, and C.-J. Lin, "Working set selection using second order information for training SVM," *J. Mach. Learn. Res.*, vol. 6, pp. 1889–1918, 2005.
[31] B. Schölkopf and A. Smola, *Learning With Kernels—Support Vector Machines, Regularization, Optimization and Beyond*. Cambridge, MA, USA: MIT Press, 2001.
[32] J. A. Tropp and A. C. Gilbert, "Signal recovery from random measurements via orthogonal matching pursuit," *IEEE Trans. Inf. Theory*, vol. 53, no. 12, pp. 4655–4666, Dec. 2007.
[33] Q. Ling, Y. Guo, Z. Lin, and W. An, "A constrained sparse representation model for hyperspectral anomaly detection," *IEEE Trans. Geosci. Remote Sens.*, vol. 57, no. 4, pp. 2358–2371, Apr. 2019.
[34] S. Boyd and L. Vandenberghe, *Convex Optimization*. Cambridge, MA, USA: Cambridge Univ. Press, 2004.
[35] J. C. Platt, *Fast Training of Support Vector Machines Using Sequential Minimal Optimization*. Cambridge, MA, USA: MIT Press, 1999.
[36] A. Giannandrea *et al.*, "The SHARE 2012 data campaign," *Proc. SPIE*, 2013, vol. 8743, Art. no. 87430F.
[37] S. Matteoli, M. Diani, and J. Theiler, "An overview of background modeling for detection of targets and anomalies in hyperspectral remotely sensed imagery," *IEEE J. Sel. Topics Appl. Earth Observ. Remote Sens.*, vol. 7, no. 6, pp. 2317–2336, Jun. 2014.
[38] J. Kerekes, "Receiver operating characteristic curve confidence intervals and regions," *IEEE Geosci. Remote Sens. Lett.*, vol. 5, no. 2, pp. 251–255, Apr. 2008.
[39] H. Kwon and N. M. Nasrabadi, "A comparative analysis of kernel subspace target detectors for hyperspectral imagery," *EURASIP J. Adv. Signal Process.*, vol. 2007, no. 1, pp. 1–13, Jan. 2006.
[40] J. M. Bioucas-Dias *et al.*, "Hyperspectral unmixing overview: Geometrical, statistical, and sparse regression-based approaches," *IEEE J. Sel. Topics Appl. Earth Observ. Remote Sens.*, vol. 5, no. 2, pp. 354–379, Apr. 2012.
[41] M. Parente and M.-D. Iordache, "Sparse unmixing of hyperspectral data: The legacy of SUnSAL," in *Proc. IEEE Int. Geosci. Remote Sens. Symp.*, 2021, pp. 21–24.
[42] A. Zare, P. Gader, and G. Casella, "Sampling piecewise convex unmixing and endmember extraction," *IEEE Trans. Geosci. Remote Sens.*, vol. 51, no. 3, pp. 1655–1665, Mar. 2013.
[43] J. M. P. Nascimento and J. M. B. Dias, "Vertex component analysis: A fast algorithm to unmix hyperspectral data," *IEEE Trans. Geosci. Remote Sens.*, vol. 43, no. 4, pp. 898–910, Apr. 2005.

Qiang Ling received the B.Eng. degree in measurement engineering and the M.Eng. degree in control science and engineering from Air Force Engineering University, Xi'an, China, in 2013 and 2016, respectively, and the Ph.D. degree in information and communication engineering from the National University of Defense Technology (NUDT), Changsha, China, in 2019.

He is currently a Lecturer with the College of Electronic Science and Technology, NUDT. His research interests include pattern recognition and hyperspectral image processing.

Kun Li received the B.S. degree in computer science and technology from the China University of Mining and Technology, Xuzhou, China, in 2007, and the M.S. degree in computer application technology from the Tianjin University of Technology, Tianjin, China, in 2010. He is currently working toward the Ph.D. degree with the College of Electronic Science and Technology, National University of Defense Technology, Changsha, China.

His research interests include pattern recognition and hyperspectral image processing.

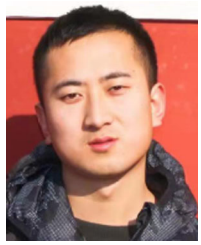

Zhaoxu Li received the B.Eng. degree in communication engineering and M.Eng. degree in information and communication engineering from the National University of Defense Technology, Changsha, China, in 2018 and 2020, respectively. He is currently working toward the Ph.D. degree with the College of Electronic Science and Technology, National University of Defense Technology, Changsha, China.

His research interests include pattern recognition, machine learning, and hyperspectral image process.

Zaiping Lin received the B.Eng. and Ph.D. degrees in information and communication engineering from the National University of Defense Technology (NUDT), Changsha, China, in 2007 and 2012, respectively.

He is currently an Associate Professor with the College of Electronic Science and Technology, NUDT. His research interests include infrared image processing and signal proces.

Jiawen Wang received the M.Eng. degree in navigation guidance and control from the Nanjing University of Aeronautics and Astronautics, Nanjing, China, in 2012.

She is currently an Engineer with the Shanghai Satellite Engineering Research Institute, China Aerospace Science and Technology Corporation, Shanghai, China. Her research interests include the overall design of optical remote sensing satellite and hyperspectral detection technology.